



Compacted bentonite hydro-mechanical modelling when interaggregate porosity tends to zero

Vicente Navarro¹ · Laura Asensio¹ · Virginia Cabrera¹ · Gema De la Morena¹ · Ángel Yustres¹ · Joel Torres-Serra¹

Received: 17 August 2022 / Accepted: 27 April 2023
© The Author(s) 2023

Abstract

A formulation is proposed for reproducing the hydro-mechanical behaviour of compacted bentonites as interaggregate porosity becomes negligible. In that case, the model assumes the bentonite deformability to be controlled only by the microstructural modelling level in a double porosity approach. Hence, the bulk stiffness of the system is defined by the relationship between the microstructural void ratio and the thermodynamic swelling pressure, requiring no additional parameters to simulate the overall behaviour. An experimental study has been conducted to check the conceptual consistency of the formulation, with favourable results. The quantitative potential of the model has also been satisfactorily verified by numerical simulation of the tests carried out in this study. A displacement-based finite-element model developed for double porosity systems has been modified to run the simulations. The proposed formulation has been implemented using a simple strategy that can be easily replicated for similar numerical models. Both the simulation capabilities and the computational cost efficiency of the proposed formulation confirm its practical interest.

Keywords Compacted bentonite · Interaggregate porosity · Macroscopic model · Modelling levels · Macrostructure · Microstructure

Introduction

Because of its low permeability, high adsorption capacity and swelling potential (Sellin and Leupin 2013), several countries are considering the use of compacted bentonite as a barrier element in deep geological repositories for the disposal of high-level radioactive waste (Bennett and Gens 2008). To assess the long-term behaviour of these barriers, a macroscopic model of the bentonite behaviour is needed. Such models should take into account the complex internal structure of the material, which has been characterised in recent years with microstructural testing techniques. Works such as those by Monroy et al. (2010), Romero (2013), Manca et al. (2016), Sun et al. (2019), and Delage and Tessier (2021) highlight the advisability of using multiporosity macroscopic models for simulating the behaviour of compacted bentonites at engineering scale. Among these, double

porosity models have experienced major advances: see, for instance, Moyne and Murad (2003), Mainka et al. (2014), Qiao et al. (2019), and the conceptual framework provided by the Barcelona Expansive Model (BExM) (Gens and Alonso 1992; Sánchez et al. 2005, 2016; Guimarães et al. 2013; Navarro et al. 2017). The BExM assumes the existence of two overlapping distinct continuous media, namely, the macro- and microstructural modelling levels, which occupy the same spatial domain. Both continua are defined as modelling tools, more in terms of functional relations rather than based on the topology of the microstructure. As proposed by Gens and Alonso (1992), the microstructural Modelling Level (m-ML) incorporates the effect on the system of the processes occurring in the spaces occupied by non-flowing water. Essentially, the microstructure is related to the space inside the aggregates formed by clay particles. The potential effect caused by changes in the aggregate geometry is modelled at the macroscopic scale by the strain increment $d\boldsymbol{\epsilon}_m$ (stress and strain are expressed hereafter using the Voigt notation, with vector magnitudes given in boldface). The effect on the whole system of processes taking place in the remaining void space—the space between aggregates, where

✉ Vicente Navarro
vicente.navarro@uclm.es

¹ Universidad de Castilla-La Mancha, Geoenvironmental Group, Ciudad Real, Spain

water can flow under hydrodynamic gradients—is modelled at the macroscopic scale by the **Macrostructural Modelling Level (M-ML)**. Macrostructural voids are expected to reorganise with aggregate volume changes. For this reason, the model considers the existence at the macroscopic level of a strain increment $d\epsilon_{M-m}$ induced by $d\epsilon_m$. In addition, even if aggregates were rigid bodies (to which the m-ML concept would not apply), their motion would also affect the arrangement of the space between them (macrostructural voids) generating the macroscale strains modelled in isothermal conditions by the Barcelona Basic Model (BBM) (Alonso et al. 1990): the elastic strain increment caused by stress changes, $d\epsilon_{M-\sigma}^e$, the elastic restructuring of the system due to suction changes, $d\epsilon_{M-s}^e$, and the plastic strains $d\epsilon_M^p$ associated with the Load-Collapse surface. An additive approach is assumed, modelling the total rearrangement of the system, $d\epsilon_r$, as

$$d\epsilon_r = d\epsilon_{M-\sigma}^e + d\epsilon_{M-s}^e + d\epsilon_M^p + d\epsilon_{M-m} + d\epsilon_m. \tag{1}$$

In problems with constant temperature and gas pressure P_G , if salinity can also be neglected, the constitutive framework allows for computing the values of $d\epsilon_{M-s}^e$, $d\epsilon_M^p$, $d\epsilon_{M-m}$, and $d\epsilon_m$ from dP_L and $d\epsilon_m$, where P_L (liquid pressure) and e_m (microstructural void ratio: volume of intra-aggregate voids per volume of minerals) are the state variables of the macro- and microstructural water mass balance equations, respectively (Navarro et al. 2019). On the other hand, the state variable of the mechanical problem in displacement-based finite-element approaches is the displacement field of the solid skeleton \mathbf{u} by which the Green–Lagrange strain is

$$\epsilon_u = \frac{1}{2} [(\nabla\mathbf{u})^t + \nabla\mathbf{u} + (\nabla\mathbf{u})^t \cdot \nabla\mathbf{u}], \tag{2}$$

where “ ∇ ” is the material gradient, and the transpose operator is denoted by superscript “ t ”. The consistency of the strains considered at both modelling levels, $d\epsilon_r$, and the strain estimated by the mechanical model, $d\epsilon_u$, implies that

$$d\epsilon_r = d\epsilon_u, \tag{3}$$

and $d\epsilon_{M-\sigma}^e$ is thereby computed as

$$d\epsilon_{M-\sigma}^e = d\epsilon_u - (d\epsilon_{M-s}^e + d\epsilon_M^p + d\epsilon_{M-m} + d\epsilon_m). \tag{4}$$

Then, $d\epsilon_{M-\sigma}^e$ can be interpreted as the “gap” between the predicted arrangement by the mechanical module ($d\epsilon_u$) and the estimated rearrangement by the constitutive formulation of the macro- and microstructural processes which are not related to the elastic strain induced by stresses ($d\epsilon_{M-s}^e + d\epsilon_M^p + d\epsilon_{M-m} + d\epsilon_m$). Assuming a model for the bulk modulus K and shear modulus G , the gap increment ($d\epsilon_{M-\sigma}^e$) is used to track the evolution of the stress state of the system. This computational scheme is applied in numerous

double porosity models (Sánchez et al. 2005, 2016; Guimarães et al. 2013; Navarro et al. 2017). However, its validity must be questioned when the macrostructural void ratio e_M (volume of inter-aggregate voids per volume of minerals) becomes small and the mechanical effect of the M-ML is negligible.

The functional “exhaustion” of the M-ML may originate for various reasons, amongst which two significant cases arise. First, as a result of mechanical loading, such as in a squeezing test, when e_M is notably reduced as compared to the microstructural void ratio e_m . Second, in swelling pressure tests, in which e_m increases under isochoric conditions thus decreasing e_M . Navarro et al. (2021) recently proposed a simulation strategy based on the assumption of the potential growth of K for e_M below a certain reference value. Although results were satisfactory in the analysed cases, the definition of K is not physically based, thus hampering the extrapolation and applicability of the approach. To circumvent this issue, the objective of the present study is to analyse in more detail the evolution of strains in bentonites for a decreasing e_M , proposing a more consistent physically based formulation. Such consistence was experimentally contrasted with a series of tests designed for this purpose. The good results obtained support the formulation. Moreover, it was implemented into a numerical model for a thorough evaluation. Satisfactory numerical results were obtained without prior parameter estimation, but using material parameters from the literature, emphasising, in consequence, the simulation capability of the proposed formulation.

Conceptual model

As e_M becomes very low, the system deformability is increasingly associated with changes in e_m . Therefore, the mechanical functionality of the M-ML is lost. The loss of some functional capacity for one of the modelling levels (loss of effect on the overall behaviour of the system) is not a novel hypothesis. All models disregarding microstructural flow are in fact assigning null hydraulic functionality to the m-ML. Yet, neglecting the hydraulic functionality in the m-ML does not deny its existence, nor its role in the stress–strain behaviour of the system, as clearly expressed in Eq. [1]. Analogously, accepting that the M-ML is irrelevant to the stress–strain behaviour of the bentonite for small e_M values does not yield the assumption of a null macrostructural hydraulic functionality. As in Navarro et al. (2021), a double porosity framework is considered, assuming that a residual macroporosity is always maintained through which some advective flow takes place, although flow through residual macroporosity is likely to be small. With keeping a double porosity model, in the proper conditions for e_M to increase, the

mechanical functionality of the M-ML is to be reactivated, recovering the modelling reasoning behind Eq. [1].

In this conceptual framework, the changes of e_m are associated with mass exchange between both modelling levels (modelled as in Navarro et al. 2021). The formulation by Coussy (2007) is then adopted, posing the Clausius–Duhem equation as

$$\sigma_{m^*} \cdot d\epsilon_{m^*} + (\mu_m - \mu_M) dn - dF \geq 0, \tag{5}$$

where $d\epsilon_{m^*}$ is the strain of the system (induced by only the m-ML), μ_m and μ_M are the chemical potentials of the water in the m-ML and M-ML, respectively, dn defines the increase of molar content of the m-ML (e_m increase is taken as positive), and dF is the variation of free energy. The system deformability being governed by the m-ML does not directly equate the strain to $d\epsilon_m$. This is the strain undergone by the system as a result of the change in volume of the aggregates when there are voids between them. When these voids are close to zero, the induced strains are likely to be different. For this reason, a strain increment $d\epsilon_{m^*}$ potentially different from $d\epsilon_m$ is considered in Eq. [5]. Assuming a saturated microstructure, and according to the proposal of Houslby and Puzrin (2000), strain work is computed using the effective stress σ_{m^*} given by

$$\sigma_{m^*} = \sigma_{TOT} - \mathbf{m} \cdot P_{m^*}, \tag{6}$$

where σ_{TOT} is the vector of total stresses, \mathbf{m} is the vector storing the identity matrix in the dimensions of stress in Voigt’s notation, and P_{m^*} is a reference pressure. To define this reference pressure, Eq. [5] is expressed in isotropic conditions:

$$p_{m^*} \cdot d\epsilon_{v-m^*} + (\mu_m - \mu_M) dn - dF \geq 0, \tag{7}$$

where p_{m^*} and $d\epsilon_{v-m^*}$ are the respective volumetric components of σ_{m^*} and $d\epsilon_{m^*}$, and $p_{m^*} = p_{TOT} - P_{m^*}$. A Lagrangian formulation is adopted, in which dF is the free energy per solid unit volume associated with a material volume, and the Clausius–Duhem equation becomes

$$- (p_{m^*} + \rho_W(\mu_M - \mu_m)) de_m - dF \geq 0, \tag{8}$$

where ρ_W is the water density. Therefore, from an energy point of view, $p_{m^*} + \rho_W(\mu_M - \mu_m)$ and e_m can be seen as conjugate magnitudes, so $p_{m^*} + \rho_W(\mu_M - \mu_m)$ can be interpreted as the constitutive stress for e_m . Navarro et al. (2018) identified this role to be played by the thermodynamic swelling pressure π and thus

$$p_{m^*} + \rho_W(\mu_M - \mu_m) = \pi, \tag{9}$$

is assumed. Defining the chemical potential of the macrostructure (Edlefsen and Anderson 1943) as

$$\mu_M = \mu_{VO} - \frac{s_M + s_{MO}}{\rho_W}, \tag{10}$$

that of the microstructure by (Anderson and Low 1957; Karnland et al. 2005)

$$\mu_m = \mu_{VO} + \frac{p - \pi - \Delta s_{mNCC}}{\rho_W}, \tag{11}$$

and from Eqs. [9–11], it results

$$P_{m^*} = P_L - (s_{MO} - \Delta s_{mNCC}), \tag{12}$$

where P_L and s_{MO} are, respectively, the pressure and osmotic suction of the aqueous solution remaining in the M-ML. Suction Δs_{mNCC} expresses the decrease in chemical potential, in units of energy per unit volume, of the microstructural water as a result of the existence of ions in excess over its cation exchange capacity, i.e., “extra” salinity due to non-charge-compensating ions. In Eqs. [10] and [11], μ_{VO} is the chemical potential of free pure water, s_M (Eq. [10]) is the macrostructural suction taken equal to the capillary suction $s_M = P_G - P_L$ (with P_G equal to the atmospheric pressure), and $p = p_{TOT} - P_G$ (Eq. [11]) is the net mean pressure.

With P_{m^*} known, σ_{m^*} is obtained with Eq. [6] and $d\epsilon_{m^*}$ is defined by

$$d\epsilon_{m^*} = \mathbf{C}_{m^*} \cdot d\sigma_{m^*}, \tag{13}$$

where the compliance matrix \mathbf{C}_{m^*} is the inverse of the stiffness matrix \mathbf{D}_{m^*} expressed as

$$\mathbf{D}_{m^*} = \begin{bmatrix} K_{m^*} & 0 \\ 0 & 3G_{m^*} \end{bmatrix}, \tag{14}$$

where the bulk modulus K_{m^*} (volumetric compressibility of the medium), defined by the state function in Fig. 1 that relates e_m and π (Navarro et al. 2017), is obtained as

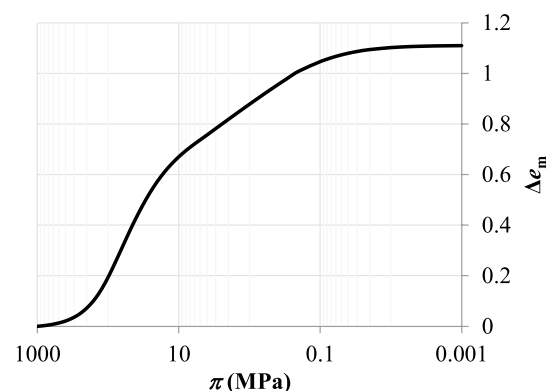


Fig. 1 State surface $e_m - \pi$ (adapted from Navarro et al. 2017)

$$K_{m^*} = \frac{d\pi}{d\varepsilon_{v-m^*}} = \frac{d\pi}{de_m} \frac{de_m}{d\varepsilon_{v-m^*}} = -(1 + e_0) \frac{d\pi}{de_m}, \tag{15}$$

being e_0 the initial value of the total void ratio ($e = e_m + e_M$: volume of voids per mineral volume), and the shear modulus is computed with the general expression:

$$G_{m^*} = \frac{3(1 - 2\nu_{m^*})}{2(1 + \nu_{m^*})} K_{m^*}. \tag{16}$$

For the sake of simplicity, Poisson’s ratio ν_{m^*} is taken equal to the value ν used to obtain the shear modulus associated with the strain $d\varepsilon_{M-\sigma}^e$. The resulting formulation does not require any additional model parameters, since both ν and the $e_m-\pi$ law are already used when Eq. [1] is valid. Conventionally, this will be accepted when the macrostructural void ratio is greater than a threshold value e_{M-T} , assuming the mechanical functionality of the M-ML to vanish for $e_M = e_{M-R}$ (residual value). A smooth transition for this process, with the subsequent activation of Eq. [13], is ensured by the transition function i_M , by means of the expression:

$$d\varepsilon_r = i_M (d\varepsilon_{M-\sigma}^e + d\varepsilon_M^p + d\varepsilon_{M-s}^e + d\varepsilon_{M-m} + d\varepsilon_m) + (1 - i_M) d\varepsilon_{m^*}, \tag{17}$$

where i_M is defined as a first approximation by a cubic Bézier curve, equal to 1 for $e_M \geq e_{M-T}$ and to 0 for $e_M \leq e_{M-R}$. Tentative values, based on the simulation of several confined swelling and squeezing tests, of $e_{M-T} = 0.02$ and $e_{M-\min 2} = e_{M-R}/10$ are considered in this work. However, the selection of these parameters will be made more accurately with broader experience in the application of the model.

As pointed out in the Introduction, the strains associated with the M-ML for $e_M \geq e_{M-R}$ are modelled with the BBM (using the formulation by Alonso et al. 2011), which relates $d\varepsilon_{M-\sigma}^e$ and the increment of net stress $d\sigma$ by

$$d\varepsilon_{M-\sigma}^e = C_M \cdot d\sigma, \tag{18}$$

where the compliance matrix C_M is the inverse of the macrostructural stiffness matrix D_M , in which the macrostructural bulk modulus is defined as

$$K_M = \frac{(1 + e_0) p}{\kappa_M}, \tag{19}$$

where κ_M is the macrostructural elastic compressibility parameter for changes in stress. Similarly, to the case of Eq. [16], the macrostructural shear modulus G_M used in D_M is calculated by

$$G_M = \frac{3(1 - 2\nu)}{2(1 + \nu)} K_M. \tag{20}$$

Then, by introducing Eqs. [13] and [18] into Eq. [17], and considering the consistency condition in Eq. [3], $d\sigma$ is defined by (see Appendix 1)

$$d\sigma = D \cdot (d\varepsilon_u - i_M \cdot d\varepsilon_{M^*}) + (1 - i_M) dP_F \cdot \mathbf{m}, \tag{21}$$

where

- (a) $d\varepsilon_{M^*} = d\varepsilon_M^p + d\varepsilon_{M-s}^e + d\varepsilon_{M-m} + d\varepsilon_m$
- (b) $dP_F = \frac{K}{K_{m^*}} (dP_{m^*} - dP_G)$
- (c) $D = \begin{bmatrix} 1/K & 0 \\ 0 & 1/(3G) \end{bmatrix}; \frac{1}{K} = \frac{1 - i_M}{K_{m^*}} + \frac{i_M}{K_M}; G = \frac{3(1 - 2\nu)}{2(1 + \nu)} K,$ (22)

Equation [21] summarises the formulation proposed in this work. It allows to integrate net stresses with a smooth transition from stress states being fundamentally controlled by the M-ML ($i_M = 1$) to being governed by the m-ML ($i_M = 0$). Equation [22] (b) defines, in turn, the change of reference pressure from P_G ($i_M = 1$) to P_{m^*} ($i_M = 0$). Once i_M is assumed, the model does not introduce parameters additional to those used in double porosity models, applied when $e_M \geq e_{M-T}$.

Model implementation

For the formulation described in Sect. “Conceptual model” to be operative, it must be implemented in a numerical module based on a double porosity approach, conceptual framework of reference. A displacement-based finite-element module is assumed, with net stress and macrostructural suction as constitutive stresses of the macrostructure (Houlsby 1997). Net stress is then originally determined from Eq. [18] by time integration of

$$d\sigma = D_M \cdot d\varepsilon_{M-\sigma}^e = D_M \cdot (d\varepsilon_u - d\varepsilon_{M^*}), \tag{23}$$

where $d\varepsilon_{M^*}$ is defined by Eq. [22] (a). As indicated by Eq. [21], the implementation of the proposed formulation will consist of the substitution of D_M by D , the introduction of i_M (function of e_M) multiplying $d\varepsilon_{M^*}$, and the addition to the stress vector of $(1 - i_M) P_F \cdot \mathbf{m}$. These are minor, easily programmable modifications that give in return a powerful tool for modelling the effect on the mechanical behaviour of the system with a progressive reduction of e_M .

The hydraulic effect can also be easily introduced. Assuming the M-ML to maintain its functionality, a transition function such as i_M is not necessary. Considering the large reduction of e_M , it is nonetheless advisable to incorporate the effect of the variation of macrostructural porosity on flow. This is usually included in the definition of intrinsic permeability, typically expressed as a function of macrostructural porosity (e.g., in Gens et al. 2011). Besides, the foreseeable effect

of large e_M variations on the macrostructural water retention properties is to be modelled by an approach such as the one proposed by De la Morena et al. (2021), Appendix 2, used in this work. Interesting complementary information on the retention properties of bentonite-based materials can be found in Fattah and Al-Lami (2016) and Fattah et al. (2017).

The retention model, together with Eqs. [21] and [22], were implemented by modifying the finite-element code used in Navarro et al. (2021), which adopts the algorithms and the hydro-mechanical formulation in Navarro et al. (2019). The latter work describes in detail the field equations used to model the flow as well as the formulation of the state functions that determine the strains defining $d\epsilon_{M^*}$. However, a brief description of these equations is given in Appendices 3 and 4. Based on this conceptual model, the numerical model was developed using the Comsol Multiphysics (COMSOL AB 2018) implementation platform, a software for solving partial differential equations by applying the Galerkin finite-element method with Lagrange multipliers. While the software offers pre-built modules, it also incorporates the "Multiphysics" capability to build modules in which the state variables can be selected, the state functions to be used can be defined, and the functional structure of the differential equations to be solved can be determined. This was the implementation strategy followed, so that the numerical model developed is adapted exactly to the formulation described in the previous section. The tailoring of the numerical formulation to the conceptual model improves its computational efficiency. Moreover, Comsol Multiphysics applies automatic symbolic differentiation techniques to obtain a high quality definition of the system iteration matrix, also contributing to improve the numerical performance of the solver. However, the application of symbolic differentiation requires that the functional dependence of the state functions used in the formulation be done carefully. Otherwise, Comsol Multiphysics is not able to apply the chain rule, cannot define the derivatives, and the calculation cannot be performed. In fact, if there are functions in which there is an implicit dependence, they must be defined as state variables of the problem to calculate their derivatives. This is the case, for example, with stresses in non-linear elastic or elastoplastic models. In this situation, as described in Navarro et al. (2014), a mixed method should be applied. However, once these problems are solved, the versatility and efficiency of the numerical tool is remarkable. The results presented in Sect. "Results and discussion" have been obtained with it.

Model inspection: experimental data

If the proposed formulation is accurate, the deformational behaviour of bentonite when e_M is reduced is expected to be controlled by the state surface in Fig. 1. Thus, it is of interest to carry out laboratory tests in which the porosity decreases

to contrast this hypothesis. To this end, ensuring maximum homogeneity of the specimen throughout the procedure, compression tests were carried out in which vertical loads were increasingly applied to bentonite samples in radial confinement conditions. Several samples at different initial dry densities and water contents were tested. For samples preparation, the bentonite was oven-dried, adding afterwards the necessary amount of deionised water to reach the target water contents. Sample homogeneity was ensured by enclosing the wetted soil in impermeable plastic film for 2 weeks under laboratory conditions, with a temperature of $23 \pm 2^\circ\text{C}$ and a relative humidity of $40 \pm 5\%$. The homogenised material was then statically compacted (see the compaction pressures in Table 1) into samples with a diameter of 36 mm and 5 mm high, using polyphenylene sulphide (PPS) ring moulds of thickness 31.85 mm to prevent radial deformation. After compaction, suction was measured using a chilled-mirror dew-point psychrometer (METER 2021), with an accuracy of ± 0.05 MPa from 0 to 5 MPa and 1% from 5 to 300 MPa of suction. Samples were then introduced into the compression equipment, based on rings of the same properties as the compaction moulds. A vertical load rate of 2.5 MPa/h was applied for 16 h, holding the final 40 MPa load for 8 h more. During the experiments, vertical displacement was measured independently from the readings of the press using a digital dial indicator with an accuracy of 2.5 μm (Hoffmann 2021). Suctions were measured again at the end of the test. The obtained results are shown in Table 1. The same Wyoming bentonite tested in Navarro et al. (2017) was used for this study, similar to the Be-Wy-BT007-1-Sa-R bentonite characterised by Kiviranta and Kumpulainen (2011), the main properties of which are summarised in Table 2.

The experimental data in Table 1 corresponds to each sample as a whole. However, the analysis of results regarding their spatially distributed behaviour is also of interest, although information of this kind is scarce. In that sense, the hydration tests reported by Massat et al. (2016) constitute a valuable contribution, as it reports in a distributed (for different points of the sample) and continuous (for different times) way the variation of porosity. A cylindrical sample of 10 mm in diameter and height, with an average dry density of 1.47 g/cm^3 and initial water content of 6.7%, was subjected to water injection at a pressure of 50 kPa through its bottom base. Null flow through the remaining boundaries was reported. The sample was kept in isochoric conditions, and the vertical swelling pressure was measured. The cell was adapted to perform X-ray microtomography (Massat et al. 2016), giving images of voxel size 5 mm, further processed using image analysis techniques to estimate the evolution of the macrostructural porosity distribution in the sample. Amongst the tests reported, this work will analyse the results obtained under low salinity conditions (0.4 mM) (Massat et al. 2016), focusing on the process of e reduction without modelling the effect of salinity. Table 2 summarises the main

Table 1 Compression tests

Test Id	T (°C)	$\sigma_{z,COMP}$ (kPa)	ρ_{dO} (g/m ³)	w_O (%)	s_{MO} (kPa)	e_{m-1}	δ_p (mm)	e_p	δ_{MAX} (mm)	e_{m-3}	π_3 (kPa)	s_{M3} (kPa)
1	23.5	6010	1230	0.05	285,787	0.139	2.629	0.135	2.629	–	–	287,963
2	22.3	12,710	1308	0.05	279,254	0.140	2.496	0.134	2.496	–	–	278,553
3	21.3	18,490	1388	0.05	273,635	0.142	2.331	0.139	2.331	–	–	275,114
4	23.0	24,140	1468	0.05	267,798	0.143	2.165	0.141	2.165	–	–	267,655
5	21.3	32,310	1545	0.05	260,232	0.146	1.997	0.146	1.997	–	–	259,242
8	25.0	18,970	1388	0.10	90,335	0.318	1.851	0.317	1.851	–	–	90,890
9	22.5	24,920	1467	0.10	84,609	0.334	1.606	0.337	1.606	–	–	83,950
10	25.0	30,860	1546	0.10	78,957	0.352	1.351	0.356	1.351	–	–	78,871
12	24.0	10,370	1311	0.15	53,581	0.455	1.675	0.455	1.675	–	–	53,403
13	23.2	17,420	1389	0.15	46,881	0.489	1.365	0.495	1.365	–	–	46,704
15	24.9	30,240	1547	0.15	35,224	0.558	0.745	0.553	0.851	0.519	41,629	41,368
16	24.4	6050	1230	0.20	31,787	0.581	1.621	0.566	1.748	0.512	42,805	42,981
17	24.7	10,460	1311	0.20	27,747	0.610	1.335	0.591	1.518	0.518	41,786	41,510
18	22.2	18,120	1388	0.20	20,960	0.664	0.867	0.681	1.263	0.534	39,086	39,110

$\sigma_{z,COMP}$ compaction load; ρ_{dO} initial dry density; w_O initial water content; s_M suction measured with the psychrometer (O: initial, 3: after dismantling); e_{m-1} initial microstructural void ratio; δ_p plateau displacement; e_p plateau void ratio; δ_{MAX} : maximum displacement; e_{m-3} , π_3 microstructural void ratio and effective stress, respectively, at point 3 (Fig. 2)

Table 2 Characteristic properties of the analysed soils

	Wyoming	Kunipia-G
Smectite content (weight %)	87.6	95
Cation Exchange Capacity (meq/100 g)	84	115
Exchangeable cations (weight %) (Na ⁺ , K ⁺ , Ca ²⁺ , Mg ²⁺)	76, 3, 16, 5	91, 1, 8, –
Particle density (kg/m ³)	2780	2710

Wyoming bentonite data from Kiviranta and Kumpulainen (2011), Kunipia-G data from Massat et al. (2016)

characteristics of the Kunipia-G montmorillonite used in Massat et al. (2016).

Results and discussion

Delage and Tessier (2021) evidenced that compression induces the progressive reduction of the larger voids. With larger voids present, the voids in the m-ML remain practically unaltered, thus e_m remaining constant, and consequently π remains constant as well. This way, the path 1 → 2 in Fig. 2 will be initially followed in the tests, figure that is the conceptual scheme of the tests in the $e-\pi$ space. If equilibrium is assumed at the beginning of the test, $\mu_m = \mu_M$ will be met at that point, and from Eqs. [10] and [11]:

$$\pi = p + s_M + (s_{MO} - \Delta s_{mNCC}). \tag{24}$$

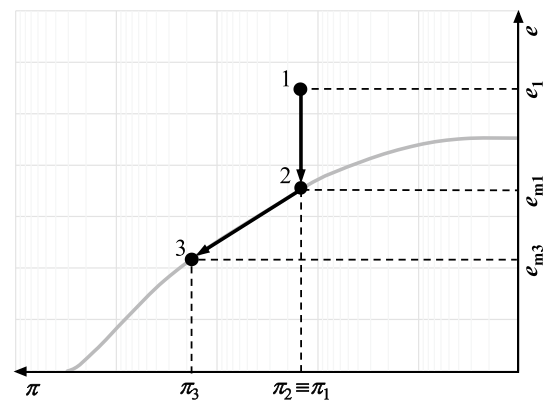


Fig. 2 Diagram of paths 1 → 2 → 3 followed in Table 1 tests within space $e-\pi$ over the reference state surface $e_m-\pi$ (grey line)

Since the initial load is null and the tests are performed under reduced salinity conditions, π can be taken equal to the initial suction in Table 1, and e_{m-1} (initial microstructural void ratio, constant along 1 → 2) can be computed from the state surface in Fig. 1. In addition, since point 2 lies on the state surface $e_m-\pi$, a significant change in the bentonite deformability is expected upon reaching that point. Further loading, after exhaustion of macropores, would follow path 2 → 3. Figure 3a represents the evolution of vertical displacement δ , positive in the loading direction, with increasing vertical pressure σ_z . A change in slope is observed after initial loading, but δ remains constant afterwards instead of

increasing with a new slope (which would be presumably smaller due to soil rigidisation along $2 \rightarrow 3$ with $e_M \approx 0$). This situation remains for the tests in Fig. 3b, whereas the tests in Fig. 3c show a second δ increase after the plateau, albeit with a reduced slope compared to the initial slope. The values of δ_p on the plateau (Table 1) are used in the calculation of the corresponding void ratio e_p , which are practically equivalent to e_{m-1} , as can be seen in Fig. 4. All tests are represented in Fig. 4, although many of the points overlap. For the tests in Fig. 3b, suction at the end of the experiments was also very similar to the initial values, see Table 1. It is hence reasonable to assume that the plateau identifies point 2 in Fig. 2.

After reaching point 2, the values of σ_z are those corresponding to the plateau in Fig. 3, and, assuming a coefficient of earth pressure at rest of

$$k_0 = \frac{\nu}{1 - \nu}, \tag{25}$$

the increase in net mean stress on the plateau can be estimated, where because δ is constant, e , and thus e_m , will not change. Since e_m in 2 is the same as in 1, according to Fig. 1, the microstructural effective stress π will also be the same. Excluding the effect of salinity, the variation of s_M is defined by p , π , and Eq. [24]. Even taking into account the simplification introduced by Eq. [25], these calculations show very high suction values on the plateau for the results in Fig. 3b. The bentonite is initially in dry conditions, and even though the increase in p leads to a reduction of s_M as a consequence

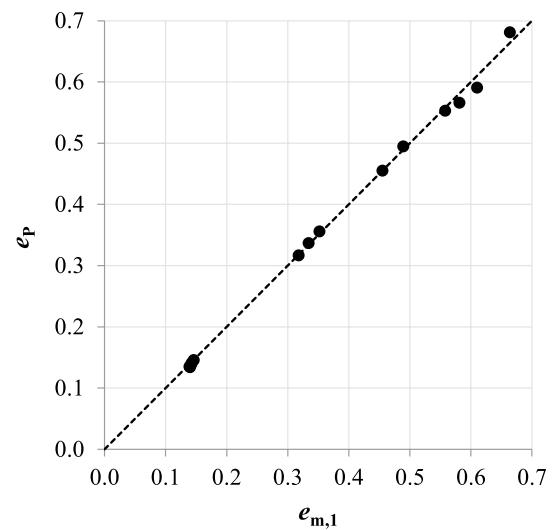


Fig. 4 Comparison of e_p vs e_{m-1}

of a decreasing e_M , suction is still high. There is no drainage, and when $e_M \approx 0$ is reached (point 2), the system shows an isochoric “undrained” behaviour. Contrarily, the tests in Fig. 3 c have larger initial water contents and, after some loading, suction is reduced enough for the bentonite to start draining and deforming, originating the second stage of increase in vertical displacement. In it, deformability is governed by the e_m reduction and the behaviour is stiffer

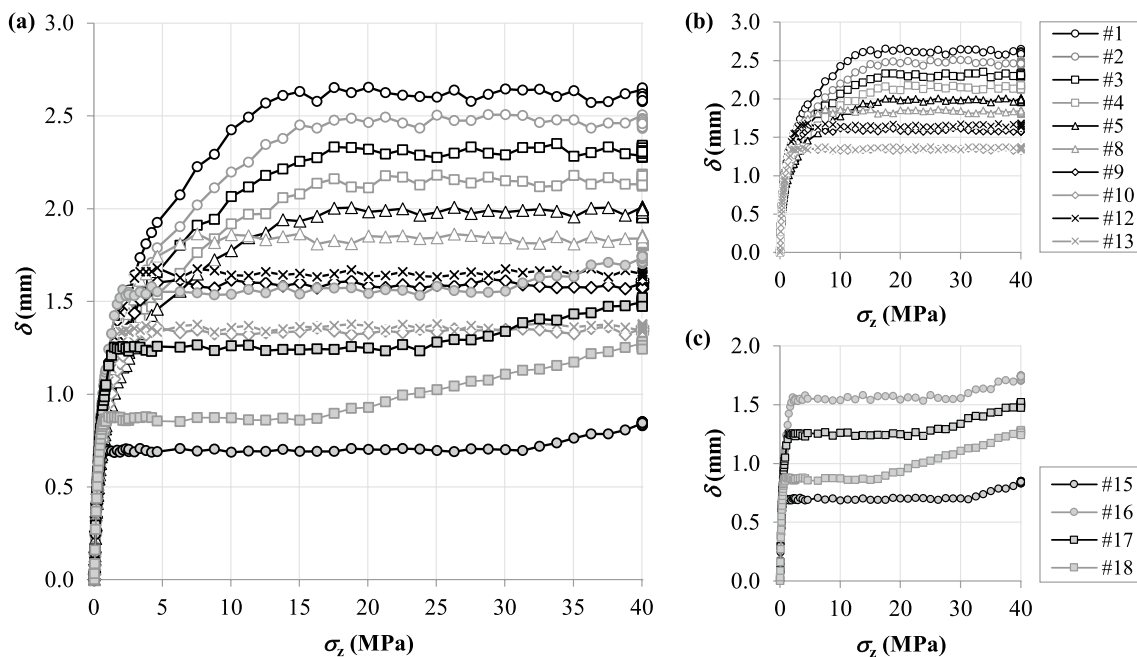


Fig. 3 Evolution of the vertical displacement δ with increasing vertical pressure σ_z . **a** All of the tests in Table 1. **b** Tests in which δ stabilises after reaching a plateau. **c** Tests experiencing a second increase of δ

than in the first increase, where deformability is associated with the reduction of e_M .

For the tests in Fig. 3c, the value of δ allows to define the reduction of e_m from point 2 onwards. Since e_m on 2 is equal to e_{m-1} , the change of e_m from there determines its total value, and then, using Fig. 1, the thermodynamic swelling pressure can be obtained in $2 \rightarrow 3$. Particularly, the values of e_{m-3} and π_3 at the end of the experiment, before dismantling the sample from the testing equipment, can be calculated (Table 1). If the operation is swiftly carried out and the sample suction s_{M3} is measured right after the dismantlement, according to Eq. [24] it must be equal to π_3 for $p=0$ after unloading. Figure 5 confirms the good correlation between π_3 and s_{M3} , corroborating the conceptual model sketched in Fig. 2 and thus underpinning the formulation proposed in this work.

Once the conceptual consistency of the formulation is confirmed, it is of interest to improve the characterisation of the simulation capability of the proposed numerical model. Tests numbers #1, #10, #16, and #18 were chosen as representative study cases. As noted above, the Wyoming bentonite used in the experiments presented is the same used in Navarro et al. (2017), Navarro et al. (2016) and Sane et al. (2013).

Therefore, except for the net mean preconsolidation stress at zero suction, the mechanical parameters estimated by Navarro et al. (2016) from the tests of Sane et al. (2013) have been used, see Table 3. Both the preconsolidation stress and the permeability parameters have been taken as those identified by Navarro et al. (2017) when analysing the experimental results of Sane et al. (2013) with an improved swelling model with respect to the one used in Navarro et al. (2016). Table 3 also includes the micro–macro–mass exchange parameters taken from Navarro et al. (2016) and the M–ML retention properties for a Wyoming bentonite from De la Morena et al. (2021). Regarding the material

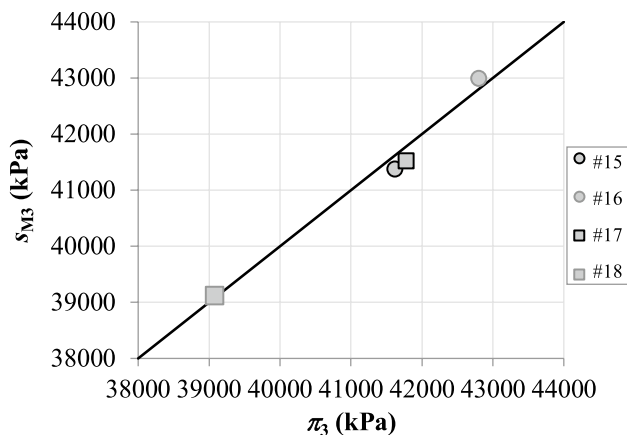


Fig. 5 Correlation between π_3 and s_{M3}

characterisation, the e_m – π state surface in Fig. 1 was used (Navarro et al. 2017).

Free vertical and null radial displacements (“roller” boundary condition in the mechanical problem) were assumed on the lateral boundaries of the sample for the simulations. Furthermore, the bottom boundary displacements were also constrained vertically, and, in accordance with the test, a load increment of 2.5 MPa/h was applied on the top boundary for the first 16 h of testing, keeping the final 40 MPa load for the remaining 8 h of simulation (test duration of 24 h). For the hydraulic simulation, the lateral boundaries were considered impervious, while seepage boundary conditions (Neuman and Witherspoon 1970) were imposed at the top and bottom boundaries. Initial conditions were taken consistently with the dry density and water content values in Table 1.

Figure 6 depicts the experimental and numerical results of the evolution of δ vs σ_z . Notable fit is observed given that the parameters used were directly taken from previous works without any kind of parameter estimation (the parameters used are completely independent of the test simulated). Not only the transition around point 2 in Fig. 3 is correctly simulated, but also the soil behaviour along path $2 \rightarrow 3$ is reasonably reproduced. In this regard, Fig. 7 shows the paths followed in the e – π space, and Fig. 8 represents the time evolution of e , e_M , and e_m (where, for the sake of clarity, only the results of simulations #1 and #18 are shown). Figures 7 and 8 show modelling results on points at $\frac{1}{4}$, $\frac{1}{2}$, and $\frac{3}{4}$ of the sample height, namely, PA (1.25 mm), PB (2.50 mm), and PC (3.75 mm), although the values obtained at different heights are indistinguishable as they overlap. A sub-vertical path in e – π is observed (Fig. 7), while M–ML is relevant (see Fig. 8: $e_M > e_{M-T}$), the system behaviour smoothly shifting to being controlled by the e_m – π state surface. Interestingly, in the no-flow or extremely reduced flow conditions of the problem, a homogeneous response of the sample is found, as implicitly assumed in Figs. 4 and 5, and for the calculated values in Table 1.

Finally, the evaluation of the conceptual and numerical formulations was completed with the simulation of the hydration test by Massat et al. (2016), described in Sect. “Model inspection: experimental data”. This is a very demanding simulation involving the characterization of the spatially and temporally distributed soil behaviour. A no normal displacement mechanical boundary condition is imposed on all boundaries. Furthermore, top and lateral impervious boundaries were considered, applying (as in the test) a 50 kPa pressure on the bottom boundary of the cylindrical sample. A homogeneous initial water content of 6.7% was taken, and a linear vertical variation of the dry density idealising the variation of macrostructural initial porosity identified in Massat et al. (2016) was adopted, as shown in Fig. 9. This figure shows the evolution of the vertical profile of macrostructural porosity with time, comparing

Table 3 Mechanical and hydraulic parameters used in the simulations

Mechanical parameters		Value	Source
k	Increase in cohesion with suction	0.1	A
κ_{iO} (1)	Saturated elastic stiffness for changes in p	0.1	A
κ_{iO} (2)	Saturated elastic stiffness for changes in p	1.1	A
α_i (MPa ⁻¹)	Parameter of the elastic stiffness for changes in p	0	A
κ_{so}	Parameter of the elastic stiffness for changes in s_M	0.05	A
α_{sp}	Parameter of the elastic stiffness for changes in s_M	0	A
α_{ss} (MPa ⁻¹)	Parameter of the elastic stiffness for changes in s_M	0	A
p_{REF} (MPa)	Parameter of the elastic stiffness for changes in s_M	0.01	A
ν	Poisson's ratio	0.35	A
p_C (MPa)	Reference stress of the net mean yield stress	0.01	A
λ_0	Slope of the virgin compression curve for saturated conditions	0.15	A
r	Parameter of the macrostructural soil compressibility	0.8	A
β (MPa ⁻¹)	Parameter of the macrostructural soil compressibility	$2.0 \cdot 10^{-2}$	A
p_{O^*} (MPa)	Net mean preconsolidation stress at zero suction	1.5	B
M	Slope of the critical state line	1.07	A
<i>Macro-micro-mass exchange parameters</i>			
C	Clay aggregate structure effect	0.4	A
H ((MPa·s) ⁻¹)	Mass-transfer connectivity	$1.5 \cdot 10^{-5}$	A
<i>Permeability parameters</i>			
b_M	Intrinsic permeability parameter	9.911	B
n_{MO}	Intrinsic permeability parameter	0.047	B
k_o (m ²)	Intrinsic permeability parameter	$2.34 \cdot 10^{-21}$	B
<i>Retention parameters (1)</i>			
λ_M	De la Morena et al. (2021) parameter	0.904	C
β_M (MPa)	De la Morena et al. (2021) parameter	0.278	C
m_M	De la Morena et al. (2021) parameter	1	C
<i>Retention parameters (2)</i>			
m	van Genuchten (1980) parameter	0.51	D
α_M (MPa ⁻¹)	van Genuchten (1980) parameter	0.389	D

The data identified by “(1)” was used to simulate the tests in Table 1, whereas the data identified by “(2)” was employed in the simulation of the test by Massat et al. (2016). Unlabelled data were used for both simulations. Source indicated in the last column (Navarro et al. 2016; Navarro et al. 2017; De la Morera et al. 2021; Navarro et al. 2021)

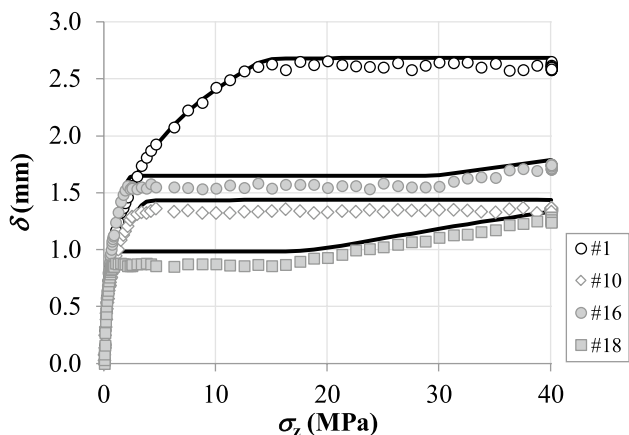


Fig. 6 Comparison between experimental values (markers) and the numerical model results (solid lines) of the evolution of δ vs σ_z

experimental values with the obtained results in this work and in Navarro et al. (2021), both using the mechanical and permeability properties in Table 3. Water retention properties (van Genuchten 1980) and the state surface $e_m - \pi$ were all derived from experimental results on Kunipia-G montmorillonite (Sato 2008). Please refer to Navarro et al. (2021) for further details. Both models produce comparable goodness of fit to the experimental data. Therefore, even with fewer parameters (the maximum stiffness of the system is not introduced independently), the new formulation is able to satisfactorily reproduce the test by Massat et al. (2016), which reinforces the validity of the proposed formulation.

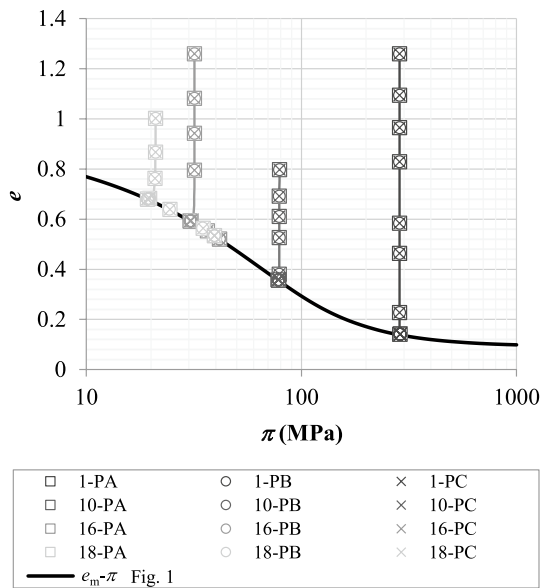


Fig. 7 Numerical simulation of paths 1 → 2 → 3 within the $e-\pi$ space of points PA, PB, and PC. The numbering in first place in the legend indicates the simulated tests from Table 1. For clarity, not all the points obtained in the simulations are represented with a marker

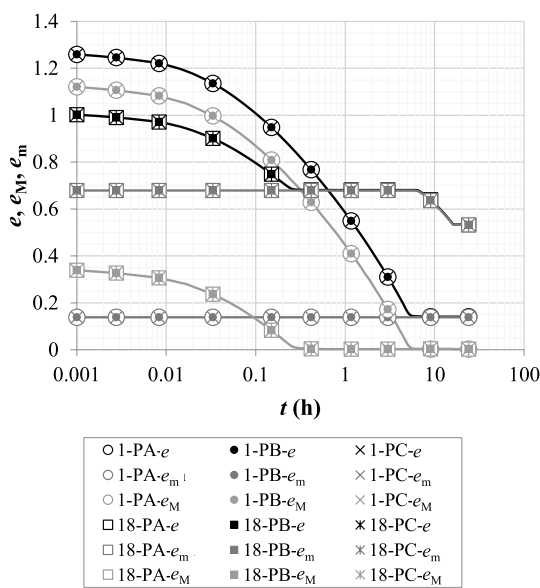


Fig. 8 Numerical simulation of the time evolution of e , e_M , and e_m of points PA, PB, and PC. The numbering in first place in the legend indicates the simulated tests from Table 1. For clarity, not all the points obtained in the simulations are represented with a marker

Conclusions

A formulation has been proposed that models the effect of interaggregate space reduction on the hydro-mechanical behaviour of compacted bentonites. This formulation

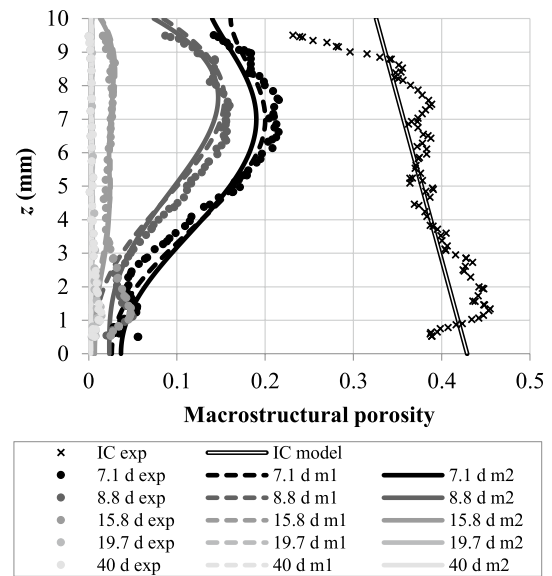


Fig. 9 Evolution of macrostructural porosity in the test analysed from Massat et al. (2016). Markers: experimental values (exp). Solid lines: results obtained with the proposed model (m2). Dashed lines: results from Navarro et al. (2021) (m1). IC: initial condition

assumes a macroscopic model of bentonite based on a double porosity approach. In it, the effects on the system of processes taking place in the intra-aggregate space are modelled by an equivalent continuous medium, the microstructure. In this work, it is labelled as the “microstructural Modelling Level” or m-ML to highlight its role as a supporting tool in macroscopic modelling. The effect of processes occurring in the remaining pores is modelled by another overlapping continuum, the macrostructure, designated as the “Macrostructural Modelling Level” or M-ML to detach it from topological meaning.

Whenever both continua have non-negligible porosity, they contribute together to the deformability of the system while accepting that flow concentrates in the M-ML. As the porosity associated with the M-ML becomes negligible, the proposed formulation assumes a residual macrostructural porosity bearing the presumably reduced hydraulic flow in the system. Therefore, neither the M-ML vanishes nor the hydraulic functionality of m-ML is activated. However, the deformability is then governed by the m-ML and the mechanical functionality of the M-ML is deactivated through a simple transition function. In addition, a model for the deformability of the system in such conditions is introduced assuming m-ML mechanical functionality only. This model is based on the volumetric bulk stiffness of the microstructural void ratio e_m , computed from the state surface relating e_m with the thermodynamic swelling pressure π .

The progressive trend of the system towards a deformational behaviour defined by the $e_m-\pi$ relationship being the key hypothesis of the model, vertical oedometric loading

tests were conducted aiming to confirm this phenomenon. The obtained results verify the hypothesis, backing the conceptual and qualitative consistency of the formulation.

The capability of the proposed approach to quantitatively reproduce the bentonite behaviour has been also evaluated using a displacement-based finite-element model. The implementation of the proposed conceptual model has been described for numerical models based on double porosity approaches, highlighting the reduced programming effort involved. The resulting numerical model was used to simulate the experiments with satisfactory results even with material parameters obtained from previous contributions, independent from the simulated tests in this work. Similarly, reported parameters from previous works were used to simulate a swelling pressure test by Massat et al. (2016). Although a challenging simulation due to the amount of experimental data on the evolution of the macroporosity distribution in the sample, acceptable fit was again observed.

This work has dealt with isothermal problems with reduced salinity and constant gas pressure. This study should be complemented with analyses of the effects of changes in temperature, salinity and gas pressure. Despite this, the obtained results highlight the simulation capability of the formulation. For this reason, and considering that (i) the application does not require any material parameters other than those of double porosity models, and (ii) the simplicity of the numerical implementation, it can be drawn that the presented approach is of interest to simulate the behaviour of compacted bentonites when the interaggregate porosity becomes minimal.

Appendix 1

Derivation of Eq. [21]

It follows from Eqs. [3] and [17] that

$$d\epsilon_u = i_M d\epsilon_{M-\sigma}^e + (1 - i_M) d\epsilon_{m^*} + i_M (d\epsilon_M^p + d\epsilon_{M-s}^e + d\epsilon_{M-m} + d\epsilon_m), \tag{26}$$

expression which, including the definition in Eq. [22 a], can be written more compactly as

$$d\epsilon_u = i_M d\epsilon_{M-\sigma}^e + (1 - i_M) d\epsilon_{m^*} + i_M d\epsilon_{M^*}, \tag{27}$$

Introducing now Eqs. [13] and [18]

$$d\epsilon_u = i_M \mathbf{C}_M \cdot d\boldsymbol{\sigma} + (1 - i_M) \mathbf{C}_{m^*} \cdot d\boldsymbol{\sigma}_{m^*} + i_M d\epsilon_{M^*}, \tag{28}$$

Thus, with Eq. [2]

$$d\epsilon_u = i_M \mathbf{C}_M \cdot d\boldsymbol{\sigma} + (1 - i_M) \mathbf{C}_{m^*} \cdot (d\boldsymbol{\sigma}_{TOT} - dP_G \mathbf{m} - dP_{m^*} \mathbf{m} + dP_G \mathbf{m}) + i_M d\epsilon_{M^*}, \tag{29}$$

and

$$(i_M \mathbf{C}_M + (1 - i_M) \mathbf{C}_{m^*}) \cdot d\boldsymbol{\sigma} - (1 - i_M) (dP_{m^*} - dP_G) \mathbf{C}_{m^*} \cdot \mathbf{m} = d\epsilon_u - i_M d\epsilon_{M^*}, \tag{30}$$

Therefore, if, as in Eq. [22 c], the global stiffness matrix **D** is defined as

$$\mathbf{D} = (i_M \mathbf{C}_M + (1 - i_M) \mathbf{C}_{m^*})^{-1}, \tag{31}$$

(where superscript “-1” indicates the inverse matrix operator), Eq. [21] is obtained, which shows how i_M defines the smooth change of the stiffness of the system from K_M to K_{m^*} when the M-ML loses its mechanical functionality.

Appendix 2

Water retention model

Adapting the formulation of Gallipoli et al. (2015), the M-ML retention curve for the Wyoming bentonite determines the macrostructural degree of saturation Sr_M as a function of the macrostructural void ratio e_M and suction s_M (De la Morena et al. 2021):

$$Sr_M = \left(1 + \left(\frac{e_M^{1/\lambda_M}}{\beta_M} s_M \right)^{\lambda_M/m_M} \right)^{-m_M}, \tag{32}$$

where the value of the material parameters β_M , λ_M and m_M is defined in Table 3. The water retention curve for the Kunipia-G montmorillonite was characterised with a van Genuchten model (1980), using the parameters in Table 3.

Appendix 3

Field equations

Although the flow model used is described in detail in Navarro et al. (2019), the formulation used is summarised here for a more complete description of the simulations presented in the previous sections. The flow of the M-ML water mass, I_M , with respect to the displacement of the solid skeleton was modelled using an advective–diffusive model:

$$I_M = \rho_w \mathbf{q}_M + \mathbf{j}, \tag{33}$$

where \mathbf{j} is the molecular diffusion of water vapour (constant gas pressure is assumed) and \mathbf{q}_M is the specific discharge of liquid water, calculated as (Pollock 1986)

$$\mathbf{q}_M = -\frac{k_I k_r}{\mu_w} (\nabla P_L + \rho_w g \nabla z), \tag{34}$$

where P_L is the liquid pressure of the macrostructure, ∇z is the gradient of the vertical coordinate oriented upward and g is the gravitational acceleration. Using the material parameters k_o , b_M and n_{MO} from Table 3, the intrinsic permeability k_I was determined with the expression (Gens et al. 2011):

$$k_I = k_o \exp(b_M(n_M - n_{MO})), \tag{35}$$

where the macrostructural porosity n_M is given by

$$n_M = \frac{e_M}{1 + e}, \tag{36}$$

The relative permeability was calculated as (Gens et al. 2011)

$$k_r = (S_{r_M})^3, \tag{37}$$

The generalisation of Fick’s law was used to define vapour diffusion (Pollock 1986):

$$\mathbf{j} = -\tau n_M(1 - S_{r_M}) D_V (\nabla \rho_V), \tag{38}$$

where as Olivella and Gens (2000), the tortuosity to vapor flow τ is assumed equal to 1. The binary diffusion coefficient of water vapor in gas was defined as (Pollock 1986)

$$D_V = 5.9 \times 10^{-3} \frac{T^{2.3}}{P_{atm}}, \tag{39}$$

expression in which the atmospheric pressure P_{atm} must be introduced in kPa and the temperature T in K to obtain D_V in m^2/s .

To conclude with the flow formulation, the non-linear model of Alonso and Navarro (2005) was adopted to model the exchange of mass from the macrostructure to the microstructure, R_{Mm}

$$\frac{R_{Mm}}{\rho_w} = H \left(\frac{\pi_B}{\pi} \right)^C (\pi - \pi_B), \tag{40}$$

The material parameters H and C are indicated in Table 3. The function π_B should be understood as the boundary pressure exerted by the macrostructure on the microstructure. It is defined as $(p + s_M) + (s_{MO} - \Delta s_{mNCC})$ (Navarro et al. 2018). If the boundary pressure is greater than the pressure π “exerted” by the microstructure “towards” the macrostructure, e_m decreases, and water transfers from the microstructure to the macrostructure. This happens when the chemical potential of the macro

structural water is lower than that of the microstructural water.

Appendix 4

Mechanical model

As stated for the flow model, the mechanical model is also described in detail in Navarro et al. (2019). However, again for the sake of clarity, its main features are summarised here. Having defined $d\epsilon_{m^*}$, Eq. [13], and $d\epsilon_{M-\sigma}$, Eq. [18], it remains to determine how to calculate $d\epsilon_{M^p}^p$, $d\epsilon_{M-s}^e$, $d\epsilon_{M-m}$ and $d\epsilon_m$. Sections “Introduction” and “Conceptual model” indicated that, in the isothermal approach considered, the first three variables were calculated using the formulation of the BBM by Alonso et al. (2011). To define the plastic strain caused in the system by the reorganisation of the M-ML, an elliptic surface based on the loading-collapse curve from Alonso et al. (1990) was taken as the reference yield surface F :

$$F = q^2 - M^2(p + p_s)(p_O - p) = 0, \tag{41}$$

where q is the von Mises stress, M is the slope of the critical state line and p_O is the net mean preconsolidation stress for the macrostructural suction s_M , calculated as

$$p_O = p_C \left(\frac{p_O^*}{p_C} \right)^{\frac{\lambda_0 - \kappa_{iO}}{\lambda(s_M) - \kappa_{iO}}}, \tag{42}$$

where the reference net mean stress p_C , the saturated elastic stiffness for changes in net mean stress κ_{iO} , and the slope of the virgin compression line under saturated conditions λ_0 are material parameters defined in Table 3. The variation of the slope of the virgin compression curve with suction was defined as a function of material parameters r and β (Table 3) as

$$\lambda(s_M) = \lambda_0 [r + (1 - r) \exp(-\beta s_M)]. \tag{43}$$

In Eq. [42], p_O^* is the net mean preconsolidation stress at zero suction, plastic parameter of the model, whose variation is determined by the hardening law:

$$dp_O^* = \frac{(1 + e) p_O^*}{\lambda_0 - \kappa_{iO}} (d\epsilon_{V,M}^p + d\epsilon_{V,M-m}), \tag{44}$$

The initial value of p_O^* considered in the simulations is defined in Table 3. The strain increments $d\epsilon_{V,M}^p$ and $d\epsilon_{V,M-m}$ are, respectively, the volumetric components of $d\epsilon_M^p$ and $d\epsilon_{M-m}$. The first increment was calculated applying the flow rule:

$$d\epsilon_M^p = d\mu \frac{\partial F}{\partial \sigma}, \tag{45}$$

where after applying the consistency equation, the plastic multiplier was calculated as

$$d\mu = \frac{\frac{\partial F}{\partial \sigma} \cdot \mathbf{D} \cdot (d\epsilon_u - (d\epsilon_{M-s}^e + d\epsilon_{M-m} + d\epsilon_m)) + \frac{\partial F}{\partial s_M} \frac{\partial p_o^*}{\partial \epsilon_{V,M}^p} d\epsilon_{V,M-m}}{\left(\frac{\partial F}{\partial \sigma} \cdot \mathbf{D} - \frac{\partial F}{\partial p_o^*} \frac{\partial p_o^*}{\partial \epsilon_{V,M}^p} \cdot \mathbf{m}^t \right) \cdot \mathbf{n}} \tag{46}$$

All $d\epsilon_{M-m}$, $d\epsilon_m$ and $d\epsilon_{M-s}^e$ were assumed to be isotropic, defined from their volumetric component. For the first strain term, in the swelling processes analysed, its volumetric component was calculated by means of an interaction function f_1 (see, for example, Sánchez et al. 2005):

$$d\epsilon_{V,M-m} = f_1 d\epsilon_{V,m}, \tag{47}$$

where for simplicity, it was assumed that f_1 varies linearly between 1 (when the p_R/p_O ratio is equal to 0) and 0 (when p_R becomes equal to p_O). The reference pressure p_R characterises the packing of the macrostructure, and it is defined as

$$p_R = p + \frac{q^2}{M^2(p + p_S)}, \tag{48}$$

with p_S being the increase in cohesion with suction, also used in Eq. [41], defined as

$$p_S = k s_M. \tag{49}$$

On the other hand, $d\epsilon_{V,m}$, the volumetric component of $d\epsilon_m$, was computed as

$$d\epsilon_{V,m} = -\frac{de_m}{1 + e}, \tag{50}$$

where e_m and its increment were obtained with the state function defined in Fig. 1. Finally, the volumetric component the strain $d\epsilon_{M-s}^e$ was defined as

$$d\epsilon_{V,M-s} = \frac{ds_M}{K_s}, \tag{51}$$

where the modulus for changes in suction K_{Ms} is given by

$$K_s = \frac{(1 + e_o) (s_M + P_{atm})}{\kappa_s}. \tag{52}$$

The elastic compressibility parameter for changes in suction κ_{Ms} was defined using the material parameters κ_{so} , α_{sp} , α_{ss} and p_{REF} (Table 3) as

$$\kappa_s = \kappa_{so} \left(1 + \alpha_{sp} \text{Ln } s_M \left(\frac{p}{p_{REF}} \right) \right) \exp(\alpha_{sps} s_M). \tag{53}$$

Acknowledgements This publication is part of Grant PID2020-118291RB-I00 funded by MCIN/AEI/<https://doi.org/10.13039/501100011033>.

Author contributions Conceptualization: VN, LA; methodology: VN, LA, VC, GDIM, AY, JTS; formal analysis and investigation: VN, GDIM; writing—original draft preparation: VN; writing—review and editing: VN, LA, VC, AY, JTS; funding acquisition: VN, LA; resources: VN, VC, GDIM, JTS; supervision: VN. VN: VN; LA: LA; VC: VC; GDIM: GdIM; AY: ÁY; JTS: JT-S.

Funding Open Access funding provided thanks to the CRUE-CSIC agreement with Springer Nature. This publication is part of Grant PID2020-118291RB-I00 funded by MCIN/AEI/<https://doi.org/10.13039/501100011033>.

Data availability The data of the tests in Table 1, performed by the authors of the article, are available upon request. Test data from Massat et al. (2016) are taken from that article, and direct access should be requested from the authors and copyright holders of Massat et al. (2016).

Declarations

Conflict of interest The authors have no relevant financial or non-financial interests to disclose.

Open Access This article is licensed under a Creative Commons Attribution 4.0 International License, which permits use, sharing, adaptation, distribution and reproduction in any medium or format, as long as you give appropriate credit to the original author(s) and the source, provide a link to the Creative Commons licence, and indicate if changes were made. The images or other third party material in this article are included in the article’s Creative Commons licence, unless indicated otherwise in a credit line to the material. If material is not included in the article’s Creative Commons licence and your intended use is not permitted by statutory regulation or exceeds the permitted use, you will need to obtain permission directly from the copyright holder. To view a copy of this licence, visit <http://creativecommons.org/licenses/by/4.0/>.

References

Alonso EE, Navarro V (2005) Microstructural model for delayed deformation of clay: loading history effects. *Can Geotech J* 42:381–392. <https://doi.org/10.1139/t04-097>

Alonso EE, Gens A, Josa A (1990) A constitutive model for partially saturated soils. *Géotechnique* 40:405–430. <https://doi.org/10.1680/geot.1990.40.3.405>

Alonso EE, Romero E, Hoffmann C (2011) Hydromechanical behaviour of compacted granular expansive mixtures: experimental and constitutive study. *Géotechnique* 61:329–344. <https://doi.org/10.1680/geot.2011.61.4.329>

Anderson DM, Low PF (1957) Density of Water adsorbed on Wyoming Bentonite. *Nature* 180:1194. <https://doi.org/10.1038/1801194a0>

Bennett DG, Gens A (2008) Overview of European concepts for high-level waste and spent fuel disposal with special reference waste container corrosion. *J Nucl Mater* 379:1–8. <https://doi.org/10.1016/j.jnucmat.2008.06.001>

COMSOL AB (2018) Comsol multiphysics reference manual, version 5.3. COMSOL AB 564:565. https://doc.comsol.com/5.5/doc/com.comsol.help.comsol/COMSOL_ReferenceManual.pdf. Accessed Mar 2023

- Coussy O (2007) Revisiting the constitutive equations of unsaturated porous solids using a Lagrangian saturation concept. *Int J Numer Anal Methods Geomech* 31:1675–1694. <https://doi.org/10.1002/nag.613>
- De la Morena G, Navarro V, Asensio L, Gallipoli D (2021) A water retention model accounting for void ratio changes in double porosity clays. *Acta Geotech* 16:2775–2790. <https://doi.org/10.1007/s11440-020-01126-0>
- Delage P, Tessier D (2021) Macroscopic effects of nano and microscopic phenomena in clayey soils and clay rocks. *Geomech Energy Environ* 27:100177. <https://doi.org/10.1016/j.gete.2019.100177>
- Edlefsen NE, Anderson ABC (1943) Thermodynamics of soil moisture. *Hilgardia* 15:31–298. <https://doi.org/10.3733/hilg.v15n02p031>
- Fattah MY, Al-Lami AH (2016) Behavior and Characteristics of Compacted Expansive Unsaturated Bentonite-sand Mixture. *J Rock Mech Geotech Eng* 8(5):629–639. <https://doi.org/10.1016/j.jrmge.2016.02.005>
- Fattah MY, Salim NM, Irshayyid EJ (2017) Determination of the Soil-water Characteristic Curve of Unsaturated Bentonite-sand Mixtures. *Environ Earth Sci* 76:201. <https://doi.org/10.1007/s12665-017-6511-2>
- Gallipoli D, Bruno AW, D'onza F, Mancuso C (2015) A bounding surface hysteretic water retention model for deformable soils. *Géotechnique* 65:793–804. <https://doi.org/10.1680/jgeot.14.P.118>
- Gens A, Alonso EE (1992) A framework for the behaviour of unsaturated expansive clays. *Can Geotech J* 29:1013–1032. <https://doi.org/10.1139/t92-120>
- Gens A, Valleján B, Sánchez M, Imbert C, Villar MV, van Geet M (2011) Hydromechanical behaviour of a heterogeneous compacted soil: experimental observations and modelling. *Géotechnique* 61:367–386. <https://doi.org/10.1680/geot.SIP11.P.015>
- Guimarães LDON, Gens A, Sánchez M, Olivella S (2013) A chemo-mechanical constitutive model accounting for cation exchange in expansive clays. *Géotechnique* 63:221–234. <https://doi.org/10.1680/geot.SIP13.P.012>
- Hoffmann (2021) Digital-analogue dial indicator 0.0005 mm reading, Measuring range: 60 mm. Hoffmann GmbH Qualitätswerkzeuge. https://cdn.hoffmann-group.com/dsh/en-GB/dsh_en-gb_46762.pdf. Accessed Mar 2023
- Houlsby GT (1997) The work input to an unsaturated granular material. *Géotechnique* 47:193–196. <https://doi.org/10.1680/geot.1997.47.1.193>
- Houlsby GT, Puzrin AM (2000) A thermomechanical framework for constitutive models for rate-independent dissipative materials. *Int J Plasticity* 16:1017–1047. [https://doi.org/10.1016/S0749-6419\(99\)00073-X](https://doi.org/10.1016/S0749-6419(99)00073-X)
- Karnland O, Muurinen A, Karlsson F (2005) Bentonite swelling pressure in NaCl solutions—experimentally determined data and model calculations. In: Alonso EE, Ledesma A (eds) *Advances in understanding engineered clay barriers—Proceedings of the International Symposium on Large Scale Field Tests in Granite*. Taylor and Francis, London, pp 241–256
- Kiviranta L, Kumpulainen S (2011) Quality control and characterization of bentonite materials. Working Report 2011–84. Posiva, Eurajoki, Finland
- Mainka J, Murad MA, Moyne C, Lima SA (2014) A Modified Effective Stress Principle for Unsaturated Swelling Clays Derived from Microstructure. *Vadose Zone J*. <https://doi.org/10.2136/vzj2013.06.0107>
- Manca D, Ferrari A, Laloui L (2016) Fabric evolution and the related swelling behaviour of a sand/bentonite mixture upon hydro-chemo-mechanical loadings. *Géotechnique* 66:41–57. <https://doi.org/10.1680/jgeot.15.P.073>
- Massat L, Cuisinier O, Bihannic I, Claret F, Pelletier M, Masrouri F, Gaboreau S (2016) Swelling pressure development and inter-aggregate porosity evolution upon hydration of a compacted swelling clay. *Appl Clay Sci* 124–125:197–210. <https://doi.org/10.1016/j.clay.2016.01.002>
- METER (2021) WP4C, METER Group Inc. USA. http://library.metergroup.com/Manuals/20588_WP4C_Manual_Web.pdf. Accessed Mar 2023
- Monroy R, Zdravkovic L, Ridley A (2010) Evolution of microstructure in compacted London Clay during wetting and loading. *Geotechnique* 60:105–119. <https://doi.org/10.1680/geot.8.P.125>
- Moyne C, Murad M (2003) Macroscopic Behavior of Swelling Porous Media Derived from Micromechanical Analysis. *Transp Porous Media* 50:127–151. <https://doi.org/10.1023/A:1020665915480>
- Navarro V, Asensio L, Alonso J, Yustres Á, Pintado X (2014) Multiphysics implementation of advanced soil mechanics models. *Comput Geotech* 60:20–28. <https://doi.org/10.1016/j.compgeo.2014.03.012>
- Navarro V, Asensio L, Yustres Á, De la Morena G, Pintado X (2016) Swelling and mechanical erosion of MX-80 bentonite: Pinhole test simulation. *Eng Geol* 202:99–113. <https://doi.org/10.1016/j.enggeo.2016.01.005>
- Navarro V, Yustres Á, Asensio L, De la Morena G, González-Arteaga J, Laurila T, Pintado X (2017) Modelling of compacted bentonite swelling accounting for salinity effects. *Eng Geol* 223:48–58. <https://doi.org/10.1016/j.enggeo.2017.04.016>
- Navarro V, de la Morena G, González-Arteaga J, Yustres Á, Asensio L (2018) A microstructural effective stress definition for compacted active clays. *Geomech Energy Environ* 15:47–53. <https://doi.org/10.1016/j.gete.2017.11.003>
- Navarro V, Asensio L, Gharbieh H, De la Morena G, Pulkkanen VM (2019) Development of a multiphysics numerical solver for modeling the behavior of clay-based engineered barriers. *Nucl Eng Technol* 51:1047–1059. <https://doi.org/10.1016/j.net.2019.02.007>
- Navarro V, de la Morena G, Gharbieh H, González-Arteaga J, Alonso J, Pulkkanen VM, Asensio L (2021) Modeling the behavior of compacted bentonites under low porosity conditions. *Eng Geol* 293:106333. <https://doi.org/10.1016/j.enggeo.2021.106333>
- Neuman SP, Witherspoon PA (1970) Finite element method of analyzing steady seepage with a free surface. *Water Resour Res* 6(3):889–897. <https://doi.org/10.1029/WR006i003p00889>
- Olivella S, Gens A (2000) Vapour transport in low permeability unsaturated soils with capillary effects. *Transp Porous Media* 40(2):219–241. <https://doi.org/10.1023/A:1006749505937>
- Pollock DW (1986) Simulation of fluid flow and energy transport processes associated with high-level radioactive waste disposal in unsaturated alluvium. *Water Resour Res* 22(5):765–775. <https://doi.org/10.1029/WR022i005p00765>
- Qiao Y, Xiao Y, Laloui L, Ding W, He M (2019) A double-structure hydromechanical constitutive model for compacted bentonite. *Comput Geotech* 115:103173. <https://doi.org/10.1016/j.compgeo.2019.103173>
- Romero E (2013) A microstructural insight into compacted clayey soils and their hydraulic properties. *Eng Geol* 165:3–19. <https://doi.org/10.1016/j.enggeo.2013.05.024>
- Sánchez M, Gens A, do Nascimento Guimarães L, Olivella S (2005) A double structure generalized plasticity model for expansive materials. *Int J Numer Anal Methods Geomech* 29:751–787. <https://doi.org/10.1002/nag.434>
- Sánchez M, Gens A, Villar MV, Olivella S (2016) Fully Coupled Thermo-Hydro-Mechanical Double-Porosity Formulation for Unsaturated Soils. *Int J Geomech* 16:D4016015. [https://doi.org/10.1061/\(ASCE\)GM.1943-5622.0000728](https://doi.org/10.1061/(ASCE)GM.1943-5622.0000728)
- Sane P, Laurila T, Olin M, Koskinen K (2013) Current status of mechanical erosion studies of bentonite buffer. Posiva Rep 2012–45. Posiva Oy. https://www.posiva.fi/material/collections/2020112111843pos3349/eqvMGbj3k/POSIVA_2012-45.pdf. Accessed Mar 2023

- Sato H (2008) Thermodynamic model on swelling of bentonite buffer and backfill materials. *Phys Chem Earth, Parts a/b/c* 33:S538–S543. <https://doi.org/10.1016/j.pce.2008.10.022>
- Sun H, Mašín D, Najser J, Neděla V, Navrátilová E (2019) Bentonite microstructure and saturation evolution in wetting–drying cycles evaluated using ESEM, MIP and WRC measurements. *Géotechnique* 69:713–726. <https://doi.org/10.1680/jgeot.17.P.253>
- Sellin P, Leupin OX (2013) The use of clay as an engineered barrier in radioactive waste management—a review. *Clay Clay Miner* 61:477–498. <https://doi.org/10.1346/CCMN.2013.0610601>
- van Genuchten MT (1980) A closed-form equation for predicting the hydraulic conductivity of unsaturated soils. *Soil Sci Soc Am J* 44(5):892–898. <https://doi.org/10.2136/sssaj1980.03615995004400050002x>

Publisher's Note Springer Nature remains neutral with regard to jurisdictional claims in published maps and institutional affiliations.